RESEARCH ARTICLE | APRIL 05 2024

Deformation-induced HCP phase transformation of CrCoNiSi₀₃ medium-entropy alloy under high strain rate tension *⊙*

Special Collection: Era of Entropy: Synthesis, Structure, Properties, and Applications of High-Entropy Materials

Hui Chang; Tuanwei Zhang ➡ ⑩ ; Junwei Qiao ⑩ ; Peter K. Liaw ⑩ ; Zhiming Jiao; Zhiqiang Li; Long Quan; Zhihua Wang ➡ ⑩



Appl. Phys. Lett. 124, 141902 (2024) https://doi.org/10.1063/5.0202924





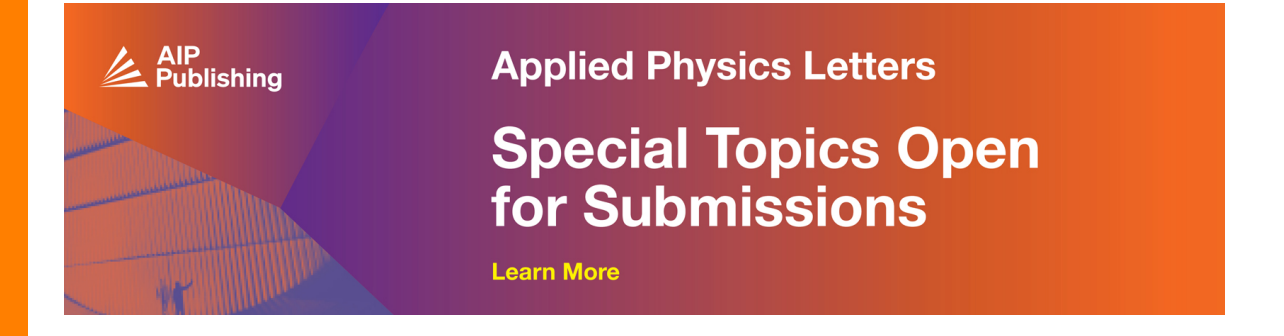
Articles You May Be Interested In

Formation and deformation mechanisms in gradient nanostructured NiCoCrFe high entropy alloys upon supersonic impacts

Appl. Phys. Lett. (November 2021)

Era of entropy: Synthesis, structure, properties, and applications of high-entropy materials

Appl. Phys. Lett. (November 2024)





Deformation-induced HCP phase transformation of CrCoNiSi_{0.3} medium-entropy alloy under high strain rate tension

Cite as: Appl. Phys. Lett. **124**, 141902 (2024); doi: 10.1063/5.0202924 Submitted: 8 February 2024 · Accepted: 21 March 2024 · Published Online: 5 April 2024







Hui Chang,¹ Tuanwei Zhang,¹.a¹ (p) Junwei Qiao,² (p) Peter K. Liaw,³ (p) Zhiming Jiao,¹ Zhiqiang Li,¹ Long Quan,⁴ and Zhihua Wang¹.a¹ (p)

AFFILIATIONS

- ¹Shanxi Key Laboratory of Material Strength and Structural Impact, College of Mechanical and Vehicle Engineering, Taiyuan University of Technology, Taiyuan 030024, China
- ²College of Materials Science and Engineering, Taiyuan University of Technology, Taiyuan 030024, China
- ³Department of Materials Science and Engineering, The University of Tennessee, Knoxville, Tennessee 37996, USA

Note: This paper is part of the APL Special Collection on Era of Entropy: Synthesis, Structure, Properties, and Applications of High Entropy Materials.

^{a)}Authors to whom correspondence should be addressed: zhangtuanwei@tyut.edu.cn and wangzh@tyut.edu.cn

ABSTRACT

The yield strength of a $CrCoNiSi_{0.3}$ medium-entropy alloy is significantly increased from 450 MPa (quasi-static, $0.001 \, s^{-1}$) to $1600 \, MPa$ (at a strain rate of $5000 \, s^{-1}$) under dynamic tension, with a considerable ductility of 60%. The high strain-rate sensitivity (SRS) of strength and work hardening is obtained, and the strength SRS reaches 0.408. The dominant deformation mechanisms are abundant multiple-twinning, increasing fractions of deformation twins and phase transformation from face-centered-cubic to hexagonal-close-packed (HCP) phases with a strain rate. A universal dislocation-hardened constitutive model considering the evolution of the twin and HCP transformation is established to predict the flow stress and microstructure evolution.

Published under an exclusive license by AIP Publishing. https://doi.org/10.1063/5.0202924

Medium/high-entropy alloys (M/HEAs) show promise for extreme environments due to their superior mechanical properties compared to conventional alloys. 1-3 Research on their tensile properties and deformation mechanisms at high strain rates is focused on a few typical FCC-based M/HEAs (CrCoNi, CrFeNi, FeCoNiCr, FeCoNiCrMn, Al_{0.1}CoCrFeNi, and Al_{0.1}Ti_{0.1}CoCrFeNi⁴⁻¹⁰) and on a limited strain rate range, leaving gaps in understanding. The M/HEAs exhibit high strain-rate sensitivity (SRS) and improved strength under dynamic tension. 4-10 The FeCoNiCr and FeCoNiCrMn HEAs exhibit the simultaneous enhancement in strength and ductility because of the formation of nanoscale deformation twins (DTs). The CrCoNi MEA is improved in both strength and ductility by the denser DTs and the appearance of multiple twinning. The deformation mechanism relates to stacking-fault energy (SFE), with lower SFE activating more mechanisms. 11,12 The CrCoNiSi_{0.3} MEA was designed for synergistic strength-ductility enhancement, with the FCC phase transforming to

the hexagonal-close-packed (HCP) phase, showing promising applications compared to CrCoNi MEA. ¹³ Consequently, the mechanical behavior and mechanisms under high-speed tension are desired to be studied.

Phenomenological and physical-based models like Johnson–Cook, Khan–Huang–Liang, and Zerilli–Armstrong lack specificity in reflecting microstructural evolution, 14,15 necessitating microstructural evolution-based constitutive models for detailed deformation mechanism understanding and alloy design guidance. The complexity of microstructural evolution in MEAs/HEAs, especially under high-speed loading, requires advanced constitutive models. $^{4-10}$ Zhang $\it et al.$ developed a dislocation-density-based hardening model for FeCoNiCr HEA. Stress models considering FCC \rightarrow BCC phase transformation was established for austenitic stainless steels 16 and $Fe_{60}Co_{15}Ni_{15}Cr_{10}$ HEA. and a crystal plasticity constitutive model containing FCC \rightarrow BCC phase transition was developed for metastable austenitic stainless

⁴Key Laboratory of Advanced Transducers and Intelligent Control System, College of Mechanical and Vehicle Engineering, Taiyuan University of Technology, Taiyuan 030024, China

steels at cryogenic temperatures. ¹⁸ However, there is a need for a constitutive model considering the FCC \rightarrow HCP transformation effect in twin-dominated MEAs/HEAs.

This study investigates dynamic tensile mechanical behaviors and strain rate effects over a wide range of strain rates on $CrCoNiSi_{0.3}$ MEA, revealing deformation mechanisms and establishing a constitutive model based on microstructural evolution and dislocation-hardening mechanism, considering $FCC \rightarrow HCP$ transformation.

The CrCoNiSi_{0,3} (in atomic proportion) and equiatomic CrCoNi (as a contrast) MEAs were prepared by vacuum arc-melting. The as-cast plates were homogenized at $1100\,^{\circ}$ C for 5 h, then cold-rolled to 70% thickness, and annealed at $900\,^{\circ}$ C for 1 h, followed by water quenching. The tensile specimens are dog-bone-shaped with the gauge geometry of $10.0 \times 4.0 \times 0.6 \, \text{mm}^3$ (quasi-static) and $4.5 \times 4.0 \times 0.6 \, \text{mm}^3$ (dynamic). Quasi-static uniaxial tensile tests were conducted with an Instron 5969 testing machine at a strain rate of $1 \times 10^{-3} \, \text{s}^{-1}$. Dynamic tension tests were performed, using a split Hopkinson tensile bar (SHTB), with postmortem measurements determining fracture strains due to large fracture strain and incomplete records.

The x-ray diffraction (XRD) measurements were performed using the BRUKER D8 diffractometer under Cu-K α radiation at 40 kV and 40 mA (scanning rate = 1° min⁻¹, $2\theta = 30^{\circ}$ - 100° , step = 0.01°). The microstructural characterizations were performed with a JEOL JSM-7100F field emission gun-scanning electron microscopy equipped with an electron backscatter diffraction (EBSD) detector and JEOL JEM-2100F transmission electron microscope (TEM).

The quasi-static tensile mechanical behaviors of CrCoNi and CrCoNiSi_{0.3} MEAs with various grain sizes are exhibited in

Figs. 1(a) and 1(b), respectively. Both MEAs show decreased strength and increased ductility with the increased grain size, according to the Hall–Petch rule, ¹⁹ while the strain hardening rate is lower especially at the beginning of the stable stage (stage II) in strain-hardening curves. More grain boundaries, rooted in smaller grain size, create more obstacles to dislocation motion, which enhances the work hardening capacity. The Hall–Petch equation is fitted to be $\sigma_y = 278.9 + 354.5 {\rm d}^{-1/2}$ and $\sigma_y = 370.3 + 462.8 {\rm d}^{-1/2}$ for the CrCoNi and CrCoNiSi_{0.3} MEAs, respectively. The lattice-friction stress and Hall–Petch slope of the CrCoNiSi_{0.3} MEA are higher than those of the CrCoNi MEA, which maybe originate from the solution strengthening of the Si element, lower SFE, and more short-range ordered domains in the CrCoNiSi_{0.3} MEA. This trend indicates that the CrCoNiSi_{0.3} MEA has a stronger grain-size effect than the CrCoNi MEA.

The tensile engineering stress–strain curves of the CrCoNi and CrCoNiSi_{0,3} MEAs at different quasi-static strain rates are shown in Figs. 1(d) and 1(e). Both MEAs showed increased strength and slightly decreased ductility with the increased strain rate since the dislocation motion had a shorter time and higher loads to overcome the obstacles. Meanwhile, the shorter plastic-deformation coordination time reduces ductility, in order to quantitatively analyze the strain-rate sensitivity (SRS), defined as $m_d = \partial \ln \sigma / \partial \ln \dot{\epsilon}$. Figure 1(f) presents the bilogarithmic diagram of the flow stress vs strain rate at various true strains. The quasi-static SRS values of the CrCoNi and CrCoNiSi_{0,3} MEAs are 0.0208 and 0.0235, respectively. The CrCoNiSi_{0,3} MEA shows a stronger SRS than the CrCoNi MEA, even exceeding the BCC-structured M/HEAs with high SRS.

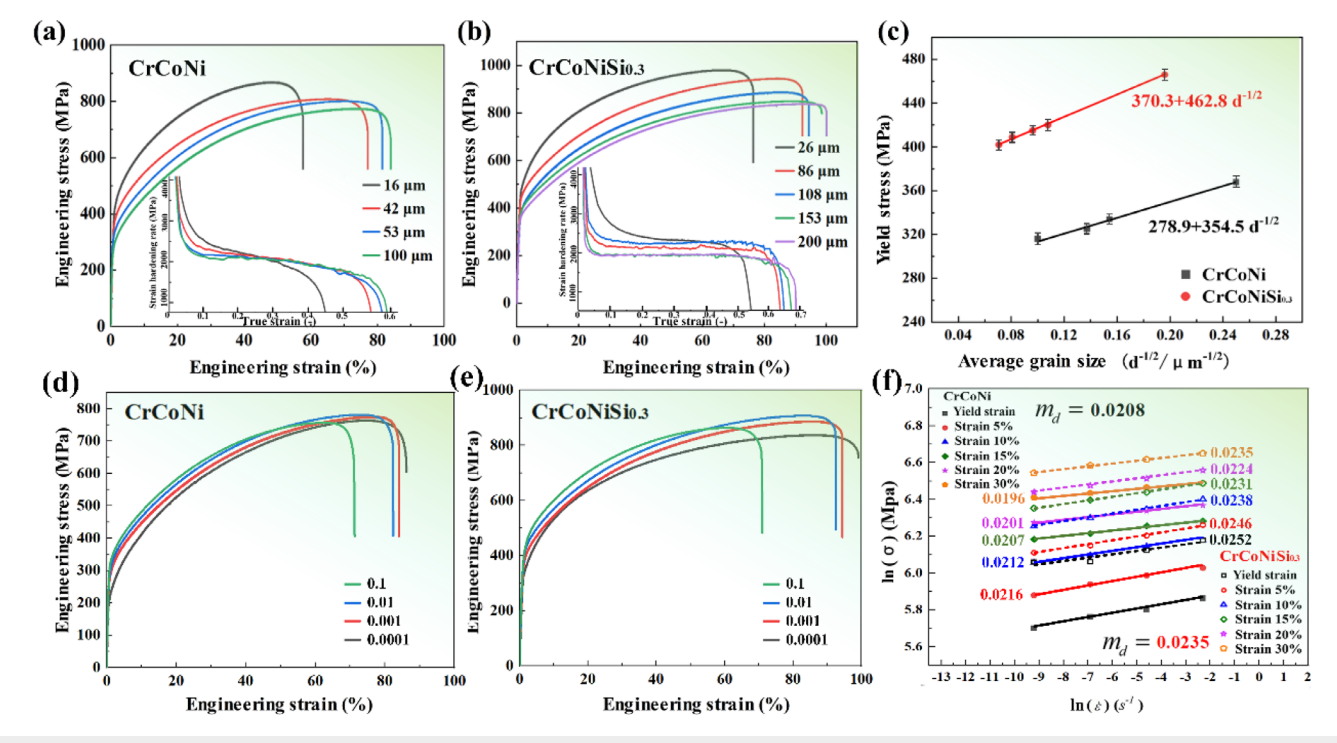


FIG. 1. (a) and (b) Quasi-static tensile mechanical behavior with corresponding strain hardening rate curves illustrated for the CrCoNi and CrCoNiSi_{0.3} MEAs with various grain sizes, respectively. (c) The Hall–Petch relationships; (d) and (e) tensile engineering stress–strain curves at different quasi-static strain rates; and (f) the bilogarithmic diagram of the flow stress vs strain rate at various true strains, showing the SRS value.

The engineering and true stress–strain curves of the CrCoNiSi_{0,3} MEA under dynamic tension are presented in Figs. 2(a) and 2(b), respectively. As the summary shown in Fig. 2(c), with increasing the strain rate from 0.001 to 5000 s⁻¹, the yield strength (σ_y) increases from 450 to 1600 MPa, the ultimate tensile strength is increased from 960 to over 2000 MPa, and the engineering fracture strain is decreased from 92% to 66%. The CrCoNiSi_{0,3} shows a similar dynamic tensile strength law to CrCoNi MEA with the increased strain rate, while their fracture elongation law is the opposite.

The SRS of the flow stress upon dynamic tension is shown in Fig. 2(d). The values of SRS under different strains are basically similar, and its average value is 0.406, which is superior to most M/HEAs, $^{4-6}$ including the CrCoNi MEA. As shown in the plot of strain-hardening components ($\sigma - \sigma_y$) vs true plastic strains at different strain rates in Fig. 2(e), the CrCoNiSi_{0.3} MEA presents an obvious and positive SRS on strain hardening capacity. The CrCoNi MEA had a higher work-hardening rate under quasi-static tension than under dynamic tension at the beginning of plastic deformation. However, the CrCoNiSi_{0.3} MEA shows consistently a higher strain-hardening component under

dynamic tension probably stemming from the lower SFE, ¹³ which promotes twinning earlier and improves the work hardening. Figure 2(f) gives the comparison of strain hardening for CrCoNi and CrCoNiSi_{0.3} MEAs. Visibly, the CrCoNiSi_{0.3} MEA exhibits a higher strainhardening capacity than CrCoNi MEA. Moreover, the higher SRS in the CrCoNiSi_{0.3} MEA originates from more localized plastic deformation and smaller activation volume due to its inherent chemical heterogeneity, ²¹ i.e., higher lattice distortion and chemical short-range order, than that of CrCoNi MEA. ¹³

The EBSD and TEM observations were conducted to explore the underlying deformation mechanisms of the CrCoNiSi_{0,3} MEA under dynamic tension. Figures 3(a)–3(c) and 3(d)–3(f) exhibit EBSD-IQ, phase, and KAM maps at the strain rates of 2100 and 5000 s⁻¹, respectively. The DTs' density gradually increases with the strain rate and is higher than that upon quasi-static tension. ¹³ Unlike the trace HCP content under quasi-static tension, the HCP fraction increases with increasing the strain rate under dynamic tension. Additionally, the KAM values significantly increase with the strain rate, indicating a higher dislocation density.

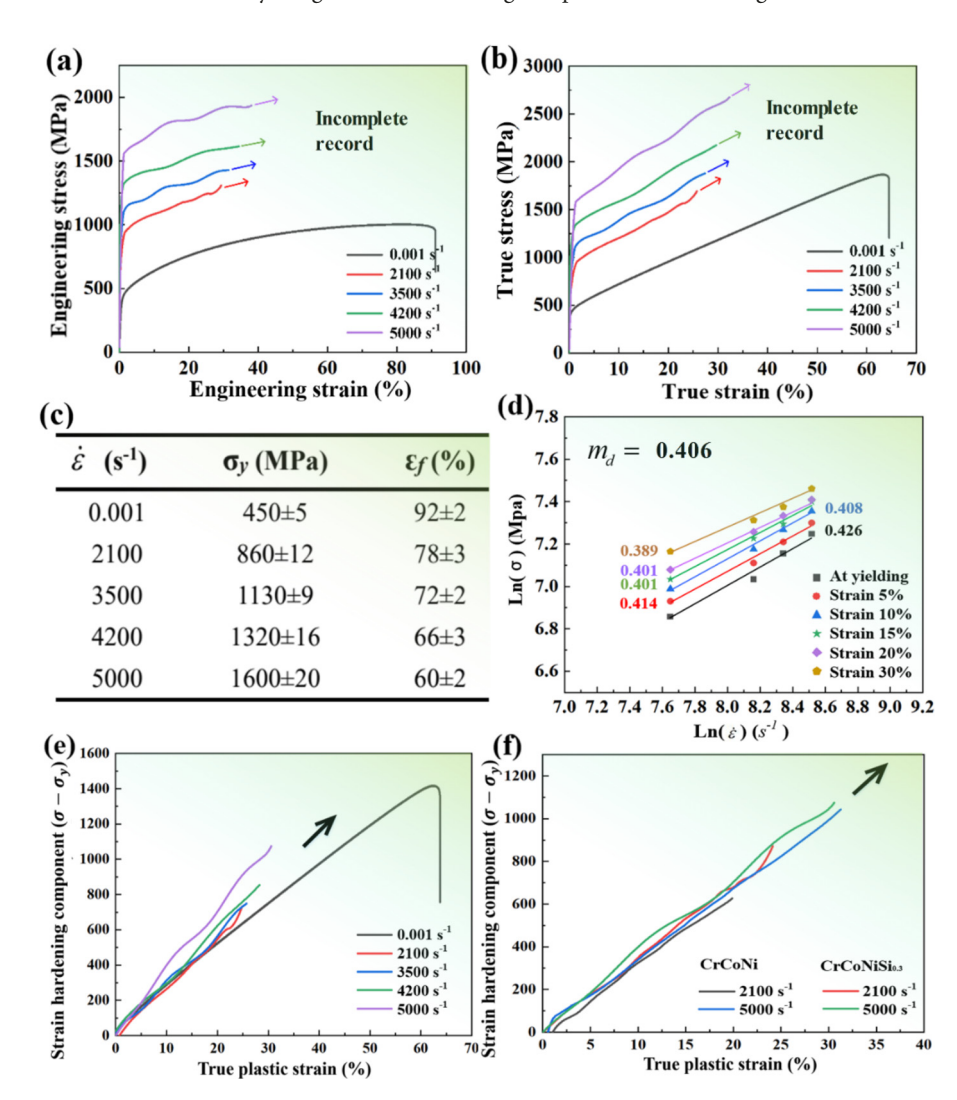


FIG. 2. (a) and (b) Engineering and true stress–strain curves for the CrCoNiSi_{0.3} MEA at different strain rates, respectively, and (c) mechanical properties summary of the CrCoNiSi_{0.3} MEA. (d) The dynamic SRS value. (e) Strain-hardening components under various strain rates. (f) Comparison of strain-hardening components between the CrCoNi and CrCoNiSi_{0.3} MEAs.

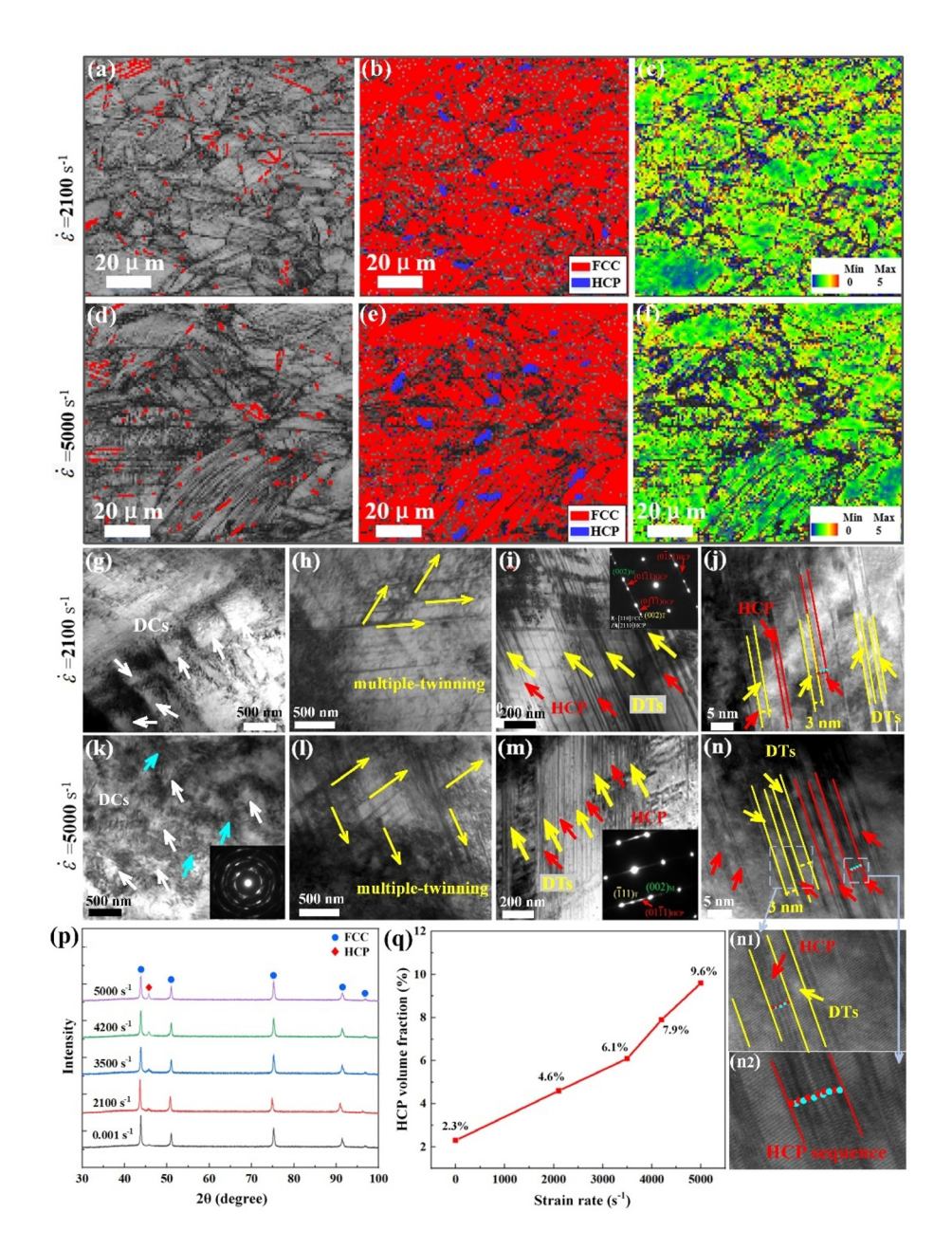


FIG. 3. Microstructures after fracture at different strain rates for the CrCoNiSi_{0.3} MEA. EBSD-IQ (a) and (d), EBSD-phase (b) and (e), and EBSD-KAM (c) and (f) maps. (g)—(n) TEM micrographs. (n1) and (n2) The corresponding enlarged image of (n). (p) The XRD patterns. (q) The volume fraction of HCP phases vs tensile strain rates.

Figures 3(g)–(j) and 3(k)–(n) exhibit the TEM micrographs after tensile fracture for the CrCoNiSi_{0.3} MEA. Dislocation cells (DCs) become denser and tighter as the strain rate increases from 2100 to 5000 s⁻¹. Specifically, a severely deformed microstructure appeared under a tensile strain at 5000 s⁻¹, as shown in the selected area diffraction patterns of the near-ring patterns in the inset of Fig. 3(k). This feature can further form nanograins. Combined with the previous nanograin formation in the CrCoNi and CoCrFeNi MEAs,^{4,22} the no appearance of nanocrystals appearance in the CrCoNiSi_{0.3} MEA maybe resulted from: (1) The hard HCP partly prevents the multiplecutting of DTs; (2) The HCP transformation consumes too much energy to provide enough energy for forming nanocrystals formation.

The formation of nanocrystals is a microscopic manifestation of softening, demonstrating a stronger hardening capacity in the present $CrCoNiSi_{0.3}$ MEA.

More abundant and denser multiple-twins are presented in the $CrCoNiSi_{0.3}$ MEA deformed at higher strain rates [Figs. 3(h) and 3(l)]. The DTs' density is obviously higher than that at quasi-static tension. Distinctly, the HCP bundles can be observed, marked by the red arrows in Figs. 3(i) and 3(m). The average twin thickness is measured to be 3 nm through the high resolution transmission electron microscope (HRTEM) images [Figs. 3(j) and 3(n) and 3(n2)], smaller than the quasi-static ones (5 nm), 13 and the thickness of the HCP sequence (AB–AB......) increases with increasing the strain rate. Consistent

with those under quasi-static tension, 13 the HCP sequence was distributed in the area of DT bundles and located in the DT-space [Figs. 3(n) and 3(n1)], indicating that the accumulation of stacking faults (SFs) at the twin boundary formed the HCP [Figs. 3(n) and 3(n2)], and the twin and SFs could be used as the nucleation sites of HCP. Furthermore, the FCC \rightarrow BCC phase transition was also found in jet penetration experiment under ultrahigh explosive loading 23 and MD simulations results at the strain rate of 10^8 s $^{-1}$ (Refs. 21 and 24) for CrCoNi MEA, but there is no BCC phase observed in the present CrCoNiSi $_{0.3}$ MEA at the present strain rate of 10^3 s $^{-1}$. The DTs fraction is estimated by combining the EBSD with TEM measurements, i.e., the product of the fraction of DTs-bundles and that of DTs in DTs-bundles. Eventually, the volume fractions of DTs are 8.9% and 9.8% at 2100 and 5000 s $^{-1}$, respectively.

In a word, with increasing the strain rate, the denser DTs, richer multiple-twinning, and more HCP transformations with increasing the strain rate together provide higher work hardening and strength, while the gradual increase in HCP phases decreases the ductility.

The XRD experiments were conducted to calculate the volume fraction of HCP phases. The HCP volume fraction can be quantitatively calculated as follows:²⁵

$$V_{\varepsilon} = \frac{\frac{1}{n} \sum_{i=1}^{n} I_{\varepsilon}^{i} / R_{\varepsilon}^{i}}{\frac{1}{n} \sum_{i=1}^{n} I_{\gamma}^{i} / R_{\gamma}^{i} + \frac{1}{n} \sum_{i=1}^{n} I_{\varepsilon}^{i} / R_{\varepsilon}^{i}},$$
(1)

where n and I represent the number of examined peaks and the integrated intensity of the diffraction peak, respectively. The material scattering factor (R) was calculated using $R = \frac{1}{v}F^2P\left(\frac{1+\cos^22\theta}{\sin\theta\sin2\theta}\right)e^{-2M}$. Here, v, F, P, e^{-2M} , and θ represent the volume of the unit cell, structure factor, multiplicity factor, temperature factor, and diffraction angle, respectively. Compared to trace HCP detection under quasistatic tension, the intensity of the ($10\bar{1}$ 1) diffraction peak gradually enhances under dynamic tension [Fig. 3(p)], and the calculated volume fraction of the HCP phase after fracture for the CrCoNiSi_{0,3} MEA aggrandizes with increasing the strain rate, as exhibited in Fig. 3(q).

The plastic deformation of metals can be regarded as the movement and accumulation of dislocations within the rate-controlled mechanism. Generally, the dislocation barriers for FCC metals could be categorized as thermal and rate-independent (i.e., athermal). ^{26,27} Correspondingly, the flow stress could be decomposed into the following:

$$\sigma = \sigma_{ath} + \sigma_{th}, \tag{2}$$

where σ is the flow stress and σ_{ath} and σ_{th} are the athermal and thermal components of the flow stress, respectively.

Grain-boundary strengthening $(\sigma_G = kd^{-1/2})$ is considered as the athermal stress, and the flow stress can be expressed as

$$\sigma = \sigma_{s}(\dot{\varepsilon}, T) + \sigma_{G} + \sigma_{H}(\varepsilon_{p}, \dot{\varepsilon}, T), \tag{3}$$

where $\sigma_s(\dot{\epsilon}, T)$ is the initial yield strength mainly from the solid solution and $\sigma_H(\varepsilon_p, \dot{\epsilon}, T)$ is the strain-hardening component.

A modified Johnson–Cook (MJ–C) model was adopted to describe σ_s to describe the high SRS of the mechanical behavior in the CrCoNiSi_{0.3} MEA,⁴

$$\sigma_s = C_1 \left[1 + C_2 \ln \frac{\dot{\varepsilon}}{\dot{\varepsilon}^*} + C_3 \left(\frac{1}{C_4 - \ln \frac{\dot{\varepsilon}}{\dot{\varepsilon}^*}} - \frac{1}{C_4} \right) \right],\tag{4}$$

where $\dot{\epsilon}^*$ is the reference strain rate (taken as 0.001 s⁻¹). C_1 , C_2 , C_3 , and C_4 are material constants and obtained as 450, 0.0172, 0.985, and 15.83, respectively. The term of $C_3\left(\frac{1}{C_4-\ln\frac{1}{\epsilon^*}}-\frac{1}{C_4}\right) \leq C_5$ can describe the increasing SRS of flow stress. The deviation in SRS is controlled by C_3 . Hence, the MJ–C model can describe materials whose σ_y deviates from the linear relationship with the logarithm of strain rate.

A Taylor-hardening model is used to reflect the flow stress during plastic deformation,²⁹

$$\sigma_H = M\alpha G b \sqrt{\rho},\tag{5}$$

where M is the Taylor factor (3.06), G is the shear modulus (86 GPa, from CrCoNi MEA³⁰), and α , ρ , and b represent the factor related to the dislocation interaction strength (0.4),⁶ total dislocation density, and the Burgers vector (0.262 nm), respectively. The evolution of total dislocation density considering the competition between the dislocation storage and recovery can be given by the following expression:

$$\frac{d\rho}{d\varepsilon_p} = M \left(\frac{1}{b\Lambda} - k_r \rho \right),\tag{6}$$

where k_r is the dislocation recovery factor and Λ is the dislocation mean free path. The main microstructure strengthening mechanisms in the present CrCoNiSi_{0.3} MEA are the DTs and HCP transformation, which play a crucial role in the evolution of dislocations. Twins and HCP phase affect dislocation evolution primarily by providing boundaries impeding dislocations motion, thus taking them into the mean free path, ^{31,32} so the expression is described as follows:

$$\frac{1}{\wedge} = k_{\rho} \sqrt{\rho} + \frac{i_{\wedge}}{\wedge_{\text{twin}}} + \frac{j_{\wedge}}{\wedge_{\text{HCP}}},\tag{7}$$

where \wedge_{twin} and \wedge_{HCP} are the mean spacing between twins and HCP islands, respectively. i_{\wedge} and j_{\wedge} are constants for scaling the contribution of the average twin spacing and average HCP path to the effective boundary distance. The mean spacing is associated with the average thickness, t, and volume fraction, F, of DTs and HCP phases,

$$\wedge = 2t \frac{1 - F}{F}.\tag{8}$$

According to twinning and phase-transition kinetics, ^{33,34} the fraction evolution of DTs and HCP phases can be expressed as

$$F_{\text{twin}} = 1 - \exp(-\phi(\varepsilon_p - \varepsilon_{\text{crit-twin}})), \tag{9}$$

$$F_{\text{HCP}} = 1 - \exp(-\beta (1 - \exp(-\alpha(\varepsilon_p - \varepsilon_{\text{crit-HCP}}))^n), \tag{10}$$

where $\varepsilon_{\rm crit-twin}$ and $\varepsilon_{\rm crit-HCP}$ are the initial strain for the twinning and HCP transition determined by the critical twinning stress ($\sigma_{\rm crit-twin}$) and the critical HCP stress ($\sigma_{\rm crit-HCP}$), respectively. The $\sigma_{\rm crit-twin}$ and $\sigma_{\rm crit-HCP}$ are 890 and 1340 MPa from the reference, respectively. ^{8,13} The initial strains for the twinning and HCP transition are taken from the true stress–strain curves. The $\varepsilon_{\rm crit-twin}$ is determined to be 0.16 and 0.02 true strains at 0.001 and 1200 s⁻¹ strain rates, respectively, and these $\varepsilon_{\rm crit-twin}$ at 2100, 3500, 4200, and 5000 s⁻¹ are consistent with

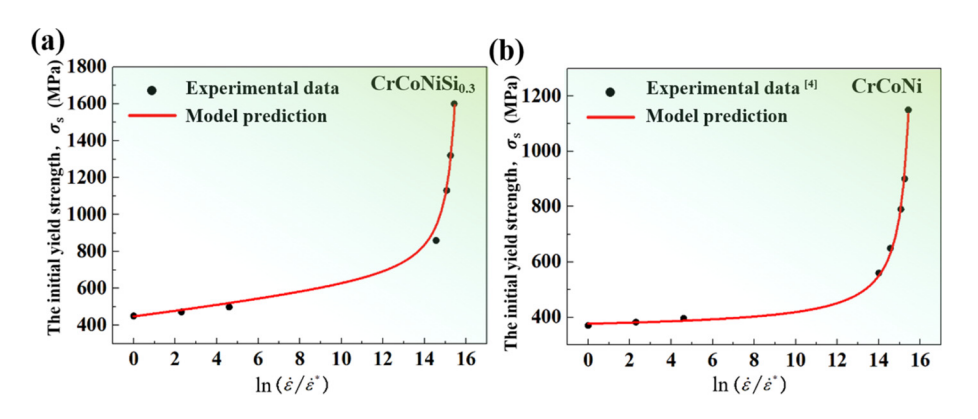


FIG. 4. Comparison of the model prediction and experimental data of $\sigma_{\rm S}$ for the CrCoNiSi_{0.3} (a) and CrCoNi $^{\rm 4}$ (b) MEAs.

the yield strain. The $\varepsilon_{\text{crit-HCP}}$ is 0.3, 0.23, 0.17, and 0.06, respectively, for the strain rates of 0.001, 1200, 2100, and 3500 s⁻¹, and the $\varepsilon_{\text{crit-HCP}}$ at 4200 and 5000 s⁻¹ is the yield strain. The fitted value of the twinevolution parameter (ϕ) is 0.185. The values of HCP evolution parameters β , α , and n fitted using experimental results are 2.01, 13.2, and 4.2, respectively.

The dislocation recovery, a thermally activated process due to its nature of dislocation motion and its sensitivity to the temperature and strain rate, is expressed as follows:³⁴

$$k_r = k_{r_0} \left(\frac{\dot{\varepsilon}}{\dot{\varepsilon}^*}\right)^{-\frac{kT}{A}},\tag{11}$$

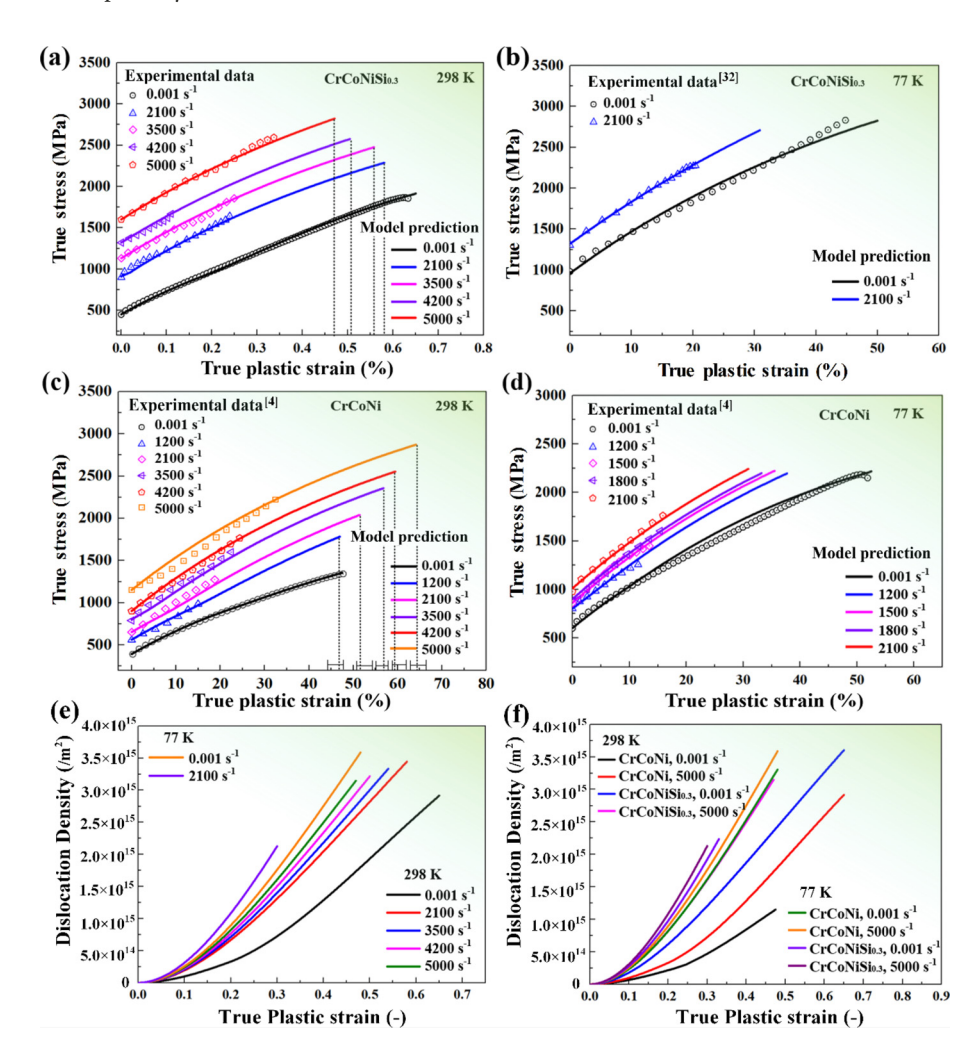


FIG. 5. Comparison of the constitutive model prediction and experimental data of the CrCoNiSi_{0.3}³⁷ (a) and (b) and CrCoNi⁴ (c) and (d) MEAs^{4,37} under different strain rates at room and cryogenic temperature. (d) The prediction of dislocation density evolution for the CrCoNiSi_{0.3} MEA and (e) the comparison of two alloys.

where k_{r_0} is the recovery factor at 0 K and k is the Boltzmann constant. Here, the reference strain rate, $\dot{\epsilon}^*$, is taken as 10^7 s⁻¹, and k is a material parameter dependent on the SFE (calculated to be 3.08×10^{-19} J). The fitted parameters of k_{r_0} are 0.017 and 0.020 under quasi-static and dynamic tension, respectively.

During dynamic deformation, the adiabatic temperature rise, which significantly affects the dislocation evolution, is defined as³⁵

$$\Delta T = T - T_0 = \frac{\eta}{\rho C_v} \int_0^{\varepsilon_p} \sigma d\varepsilon, \tag{12}$$

where T_0 is the initial temperature (298 K), T is the current transient temperature, ΔT is the temperature rise, ρ is the mass density of the alloy (7.86 g/cm³), and C_v is the specific heat capacity [452 J/ (kg K)]. 30 η is the converted fraction of the plastic work into heat (0.9). 6,36

The predicted σ_s for the CrCoNiSi_{0.3} MEA and CoCrNi MEA⁴ exhibited in Fig. 4 shows reasonable consistency with the experimental counterparts. Figure 5(a) shows that the flow-stress predictions of our model agree well with the experimental data. The dynamic-experimental data were not fully recorded, and the UTS could be predicted through the model prediction [see Fig. 5(a)]. Furthermore, the previous experimental results^{4,37} of the CoCrNi MEA and CrCoNiSi_{0.3} MEA deformed at 77 K are predicted, and the good predictions are obtained as shown in Figs. 5(b)-5(d). This feature also verifies the universal applicability of the established model where the DTs and FCC → HCP transformation are dominant mechanisms. Figures 5(e) and 5(f) show the predicted dislocation density evolution of the CrCoNiSi_{0.3} and CrCoNi MEAs during deformation. One can note that the dislocation density increases with increasing the strain rate, further underpinning the greater work hardening.

In summary, the yield strength of the $CrCoNiSi_{0.3}$ MEA is significantly increased from 450 to $1600\,MPa$ with increasing the strain rate, along with 60% ductility at $5000\,s^{-1}$, the high strength SRS, and work hardening. This trend originates from abundant multiple-twinning, increasing DTs and HCP-transformation amounts with the strain rate. A universal constitutive model is established based on the microstructure evolution.

This work was supported by the National Natural Science Foundation of China (Nos. 12072220, 12302480, 12102291, and 52271110), the Science and Technology Innovation Teams of Shanxi Province (No. 202204051002006), the National Science Foundation (DMR—1611180, 1809640, and 2226508), and the U.S. Army Research Office (W911NF-13-1-0438 and W911NF-19-2-0049).

AUTHOR DECLARATIONS Conflict of Interest

The authors have no conflicts to disclose.

Author Contributions

Hui Chang: Conceptualization (equal); Data curation (equal); Funding acquisition (equal); Investigation (equal); Methodology (equal); Visualization (equal); Writing – original draft (equal); Writing – review & editing (equal). **Tuanwei Zhang:**

Conceptualization (equal); Funding acquisition (equal); Investigation (equal); Methodology (equal); Writing – review & editing (equal). Junwei Qiao: Funding acquisition (equal); Writing – review & editing (equal). Peter K. Liaw: Funding acquisition (equal); Writing – review & editing (equal). Zhiming Jiao: Writing – review & editing (equal). Zhiming Jiao: Writing – review & editing (equal). Li: Funding acquisition (equal); Writing – review & editing (equal). Long Quan: Writing – review & editing (equal). Zhihua Wang: Funding acquisition (equal); Project administration (equal); Supervision (equal); Writing – review & editing (equal).

DATA AVAILABILITY

The data that support the findings of this study are available from the corresponding authors upon reasonable request.

REFERENCES

- ¹Y. Kimura, T. Inoue, F. X. Yin, and K. Tsuzaki, Science 320, 1057 (2008).
- ²P. Kumar, M. Kawasaki, and T. G. Langdon, J. Mater. Sci. **51**, 7–18 (2016).
- ³B. Gludovatz, A. Hohenwarter, and K. V. S. Thurston, Nat. Commun. 7, 10602 (2016).
- ⁴H. Chang, T. W. Zhang, J. J. Wang, Z. Q. Li, and Z. H. Wang, J. Mech. Eng. 58(20), 350–360 (2022).
- ⁵K. Wang, X. Jin, Y. Zhang, P. K. Liaw, and J. W. Qiao, Phys. Rev. Mater. 5, 113608 (2021).
- ⁶T. W. Zhang, S. G. Ma, D. Zhao, Y. C. Wu, Y. Zhang, Z. H. Wang, and J. W. Qiao, Int. J. Plast. **124**, 226 (2020).
- ⁷Y. Qiao, Y. Chen, F. H. Gao, H. Y. Wang, and L. H. Dai, Int. J. Impact Eng. 158, 104008 (2021).
- ⁸M. Shabani, J. Indeck, K. Hazeli, P. D. Jablonski, and G. J. Pataky, J. Mater. Eng. Perform. 28, 4348 (2019).
- ⁹K. Jiang, J. G. Li, Y. F. Meng, B. Hou, and T. Suo, Mater. Sci. Eng., A 860, 144275 (2022).
- ¹⁰Z. Tian, T. W. Zhang, Z. H. Wang, Z. H. Xie, and F. Fang, J. Alloys Compd. 968, 172092 (2023).
- ¹¹L. Y. Liu, Y. Zhang, Z. W. Zhang, J. P. Li, W. G. Jiang, and L. X. Sun, Int. J. Plast. 172, 103853 (2024).
- ¹²S. Paul and P. P. Bhattacharjee, Mater. Today Commun. 38, 107678 (2024).
- ¹³H. Chang, T. W. Zhang, S. G. Ma, D. Zhao, R. L. Xiong, T. Wang, Z. Q. Li, and Z. H. Wang, Mater. Des. 197, 109202 (2021).
- ¹⁴Z. Xu and F. Huang, Int. J. Impact Eng. **79**, 65–74 (2015).
- ¹⁵F. J. Zerilli and R. W. Armstrong, J. Appl. Phys. **61**(5), 1816 (1987).
- ¹⁶M. Mansourinejad and M. Ketabchi, Mater. Sci. Technol. 33, 1948–1954 (2017).
- ¹⁷J. Kwon, J. Lee, and H. S. Kim, Mater. Sci. Eng., A 840, 142915 (2022).
- ¹⁸M. Homayounfard and M. Ganjiani, Int. J. Impact Eng. 156, 103344 (2022).
- ¹⁹S. Yoshida, T. Bhattacharjee, Y. Bai, and N. Tsuji, Scr. Mater. 134, 33 (2017).
- ²⁰Y. Zou, J. M. Wheeler, H. Ma, P. Okle, and R. Spolenak, Nano Lett. 17(3), 1569 (2017).
- ²¹S. C. Dai, Z. C. Xie, and Y. J. Wang, Int. J. Plast. **149**, 103155 (2022).
- ²²Z. H. Wang, T. W. Zhang, E. L. Tang, R. L. Xiong, Z. M. Jiao, and J. Qiao, Appl. Phys. Lett. **119**, 201901 (2021).
- ²³ J. Chen, T. W. Liu, F. H. Cao, H. Y. Wang, Y. Chen, and L. H. Dai, Metals 12, 811 (2022).
- ²⁴F. H. Cao, Y. J. Wang, and L. H. Dai, Acta Mater. **194**, 283–294 (2020).
- ²⁵A. K. De, D. C. Murdock, M. C. Mataya, J. G. Speer, and D. K. Matlock, Scr. Mater. **50**, 1445 (2004).
- ²⁶F. C. Salvado, F. Teixeira-dias, S. M. Walley, L. J. Lea, and J. B. Cardoso, Proc. Mater. Sci. Technol. 88, 186–231 (2017).
- ²⁷K. B. Yuan, W. G. Guo, D. W. Li, P. H. Li, Y. Zhang, and P. C. Wang, Int. J. Plast. 136, 102865 (2021).
- ²⁸W. K. Rule and S. E. Jones, Int. J. Impact Eng. **21**, 609 (1998).
- ²⁹B. Hutchinson and N. Ridley, Scr. Mater. **55**, 299 (2006).

 ³⁰Z. Wu, H. Bei, G. M. Pharr, and E. P. George, Acta Mater. **81**, 428 (2014).
 ³¹J. S. Aristeidakis and G. N. Haidemenopoulos, Acta Mater. **228**, 117757 (2022).

³²Y. Kim, H. K. Park, P. Asghari-Rad, J. Jung, J. Moon, and H. S. Kim, Met. Mater. Int. 27, 2300 (2021).

³³G. B. Olson and M. Azrin, Metall. Trans. A 9, 713 (1978).

³⁴O. Bouaziz, Y. Estrin, Y. Brechet, and J. D. Embury, Scr. Mater. **63**, 477 (2010).

³⁵S. Lee and B. C. De Cooman, Metall. Mater. Trans. A 45, 709 (2014).

³⁶L. Choisez, L. Ding, M. Marteleur, H. Idrissi, T. Pardoen, and P. J. Jacques, Nat. Commun. 11, 2110 (2020).

³⁷H. Chang, T. W. Zhang, Z. Q. Li, and Z. H. Wang, "Cryogenic FCC → HCP phase transformation mechanism in low stacking fault energy medium entropy". alloy under static and dynamic tension" (unpublished).